

# Disorder-Engineered Hybrid Plasmonic Cavities for Emission Control of Defects in hBN

Sinan Genc,<sup>1,2,\*</sup> Oguzhan Yucel,<sup>2,3,\*</sup> Furkan Ađlarcı,<sup>4</sup> Carlos Rodriguez-Fernandez,<sup>5</sup>  
Alpay Yilmaz,<sup>2</sup> Humeyra Caglayan,<sup>5,6,†</sup> Serkan Ateş,<sup>4,‡</sup> and Alpan Bek<sup>2,§</sup>

<sup>1</sup>*Department of Electrical Electronics Engineering, Abdullah Gül University, 38080, Kayseri, Turkey*

<sup>2</sup>*Department of Physics, Middle East Technical University, 06800, Ankara, Turkey*

<sup>3</sup>*Department of Physics, Freie Universität Berlin, 14195, Berlin, Germany*

<sup>4</sup>*Department of Physics, İzmir Institute of Technology, 35430, İzmir, Turkey*

<sup>5</sup>*Department of Physics, Tampere University, 33720, Tampere, Finland*

<sup>6</sup>*Department of Electrical Engineering and Eindhoven Hendrik Casimir Institute, Eindhoven University of Technology, Eindhoven 5600 MB, The Netherlands*

Defect-based quantum emitters in hexagonal boron nitride (hBN) are promising building blocks for scalable quantum photonics due to their stable single-photon emission at room temperature. However, enhancing their emission intensity and controlling the decay dynamics remain significant challenges. This study demonstrates a low-cost, scalable fabrication approach to integrate plasmonic nanocavities with defect-based quantum emitters in hBN nanoflakes. Using the thermal dewetting process, we realize two distinct configurations: stochastic Ag nanoparticles (AgNPs) on hBN flakes and hybrid plasmonic nanocavities formed by AgNPs on top of hBN flakes supported on gold/silicon dioxide (Au/SiO<sub>2</sub>) substrates. While AgNPs on bare hBN yield up to a two-fold photoluminescence (PL) enhancement with reduced emitter lifetimes, the hybrid nanocavity architecture provides a dramatic, up to 100-fold PL enhancement and improved uniformity across multiple emitters, all without requiring deterministic positioning. Finite-difference time-domain (FDTD) simulations and time-resolved PL measurements confirm size-dependent control over decay dynamics and cavity-emitter interactions. Our versatile solution overcomes key quantum photonic device development challenges, including material integration, emission intensity optimization, and spectral multiplexity. Future work will explore potential applications in integrated photonic circuits hosting on-chip quantum systems and hBN-based label-free single-molecule detection through such quantum nanoantennas.

Keywords: hBN, photoluminescence, nanocavity, enhancement, dewetting.

## I. INTRODUCTION

Quantum emitters are central to quantum technologies due to their intrinsically non-classical light emission [1]. Emitters based on two-dimensional (2D) materials offer a promising platform for scalable photonic quantum technologies, owing to their compactness, stability, and tunable properties [2]. Among these materials, hexagonal boron nitride (hBN) offers several advantageous properties, such as high chemical and thermal stability [3, 4], a wide bandgap (6 eV), and the ability to host room-temperature single-photon emitters based on atomic defects [5–8]. Despite some challenges, such as defect control, spectral variability, and quantum yield limitations, advances in material synthesis, defect engineering, and nanofabrication are progressively overcoming these hurdles, paving the way for the integration of hBN into next-generation quantum photonic devices [9–11]. Overall, these properties also make hBN an attractive material for cavity systems. Its wide bandgap effectively isolates quantum emitters from environmental noise, enhancing emission stability, while its ultra-thin, atomically smooth layers enable precise control over cavity geometries [12, 13]. However, similar to the other 2D materials, the main challenges of using hBN as an emitter

in a cavity system are the precise defect placement and uniform layer thickness, which remain significant technical hurdles [14, 15]. Additionally, integrating hBN with metallic or dielectric substrates requires advanced fabrication techniques to preserve its intrinsic properties, adding complexity to the manufacturing process.

The idea of coupling a quantum emitter with a photonic cavity originates from modifying spontaneous emission by changing the environment of the quantum emitter (Purcell effect [16]), which can be used to adjust its emission characteristics. After the first experimental demonstration of modified emission from a single quantum system with a millimeter-sized cavity and with the advances in microfabrication techniques, microcavities came forth due to their comparatively diminutive volumes in the micron range, with the potential to integrate into large-scale photonic circuitry [17].

Metallic nanostructures featuring nanoscale gaps support hybrid plasmonic modes with ultra-small mode volumes and highly localized electromagnetic fields, making them ideal for exploring light-matter interactions at the nanoscale [24, 25]. Despite their potential, conventional cavity designs, such as gaps of plasmonic bowtie antennas and dielectric resonators, encounter significant constraints in practical applications. While bowtie antennas are efficient in field concentration, their fabrication is challenging due to the minuscule gap, and they often lack scalability, making them unsuitable for widespread use [26, 27]. Similarly, dielectric resonators exhibit higher mode volumes and provide less field localization and limited Purcell factor enhancement [28].

\* These authors contributed equally

† Corresponding author: hcaglayan@tue.nl

‡ Corresponding author: serkanates@iyte.edu.tr

§ Corresponding author: bek@metu.edu.tr

TABLE I. Some examples of cavity-enhanced hBN photoluminescence (PL) studies.

Enhancement Factor	Precise Location of hBN to Cavity/Nanostructure	REF
11	Emitters are located at the center of a reflective dielectric cavity for optimized reflection.	[18]
3	hBN emitters positioned near gold (Au) nanospheres using atomic force microscopy.	[19]
1.4–4.0	Emitters transferred from dielectric to metallic substrates to form a hybrid metal-dielectric structure.	[20]
250	Emitters are placed in a nano-patch antenna cavity coupled tightly to the cavity area.	[21]
8	Carbon enriched hBN layers (hBN:C) were transferred from the hBN:C crystal to a silicon dioxide/silicon (SiO <sub>2</sub> /Si) substrate.	[22]
2	Solution-synthesized Ag nanocubes are drop-casted on ion-implanted ultrathin hBN flakes on Si substrate.	[23]

Additionally, both plasmonic and dielectric systems often struggle with integration into 2D material systems due to mismatched geometries, reduced stability, and inconsistent electromagnetic coupling efficiencies [29, 30]. Alternative antenna designs, including dipole, monopole, and Yagi-Uda antennas, address some limitations but introduce their challenges. Dipole and monopole antennas, while simple and efficient, cannot localize fields at nanoscale volumes compared to plasmonic designs, limiting their effectiveness in enhancing light-matter interactions [31]. Although Yagi-Uda antennas offer excellent directional emission and gain, they are challenging to miniaturize for nanoscale systems, complicating their integration with 2D material-based quantum technologies [32, 33]. Furthermore, their alignment and coupling requirements demand precise fabrication, increasing overall complexity and cost.

Table I lists some of the plasmonic enhancement factors of hBN PL as reported in the literature. In studies concerning cavity-enhanced emission from hBN quantum emitters, enhancement factors (EF) exhibit considerable variation based on the type of cavity and the location of the emitter. Dielectric cavities often produce moderate electric field (EF) values (e.g., 11 in [18]), but plasmonic structures like nano-patch antennas can attain significantly greater enhancements (up to 250 in [21]) owing to intense field confinement and near-field coupling. Conversely, systems dependent on random nanoparticle distribution or weak hybrid interfaces frequently yield modest enhancement factors (EF < 4), highlighting the significance of accurate emitter-cavity alignment and resonant mode optimization. Similarly, dielectric optical cavities have also been used to enhance the PL of hBN [34, 35]. The recorded enhancement factors by dielectric cavities are comparable to those of the plasmonic nanocavities. One promising technique for integrating emitters with plasmonic nanostructures is the thermal dewetting of noble metal films. In this process, a thin metal film breaks up into nano-islands upon annealing, forming stochastic nanoscale antennas near the emitter locations without requiring lithography or precise placement. These disorder-engineered, self-assembled nano-antennas exhibit coupling to nearby defect emission in hBN flakes with a minimal fabrication effort.

In this study, we explore two complementary approaches to control the emission from single defects in hBN using plasmonic cavities: (i) direct formation of AgNPs via thermal

dewetting of a Ag film on hBN flakes dispersed on a Si substrate and (ii) fabrication of hybrid plasmonic nanocavities by thermal dewetting of a Ag film on hBN flakes dispersed on Au/SiO<sub>2</sub> coated Si substrates. We investigate the impact of these plasmonic configurations on key emission properties such as photoluminescence intensity, lifetime, saturation behavior, and single-photon purity through a combination of experimental measurements and FDTD simulations.

## II. RESULTS AND DISCUSSION

Figure 1a shows a typical optical image of the sample surface, where several hBN structures are clearly visible. A scanning electron microscope (SEM) image of the selected bulk hBN flakes is shown in Figure 1b. The hBN sample consists of multiple flakes with varying sizes (on the order of tens of nanometers) and orientations, which may significantly influence the optical properties of the quantum emitters present within the flakes. To investigate the spectral characteristics of these structures, a home-built micro-photoluminescence ( $\mu$ -PL) setup was employed. The details of the setup can be found in the Experimental Section.

Figure 1c shows a representative room-temperature PL spectrum of a bulk hBN flake excited with a 532 nm continuous-wave (CW) laser. The spectrum exhibits several characteristic features: a Raman peak at 547 nm corresponding to the Si substrate ( $520 \text{ cm}^{-1}$ ), and a sharp Raman peak at 574 nm ( $1370 \text{ cm}^{-1}$ ) arising from the high-energy  $E_{2g}$  phonon mode of hBN. Although hBN also possesses a low-energy Raman-active mode around  $52 \text{ cm}^{-1}$ , this feature is not visible in our measurements due to strong spectral filtering near the excitation wavelength [36–38]. A sharp emission peak centered at 684 nm, accompanied by a weaker and broader feature at 753 nm, is also observed. These are assigned to the zero-phonon line (ZPL) and its corresponding phonon sideband (PSB), respectively, originating from a single defect in hBN. The energy difference between the ZPL and PSB matches well with the energy of the high-energy phonon mode, confirming their assignment. Polarization-resolved measurements (inset of Fig. 1c) reveal strong linear polarization in both excitation (filled circles) and emission (open circles), consistent with a single dipole transition [39–41].

To confirm the quantum nature of the emission, we mea-

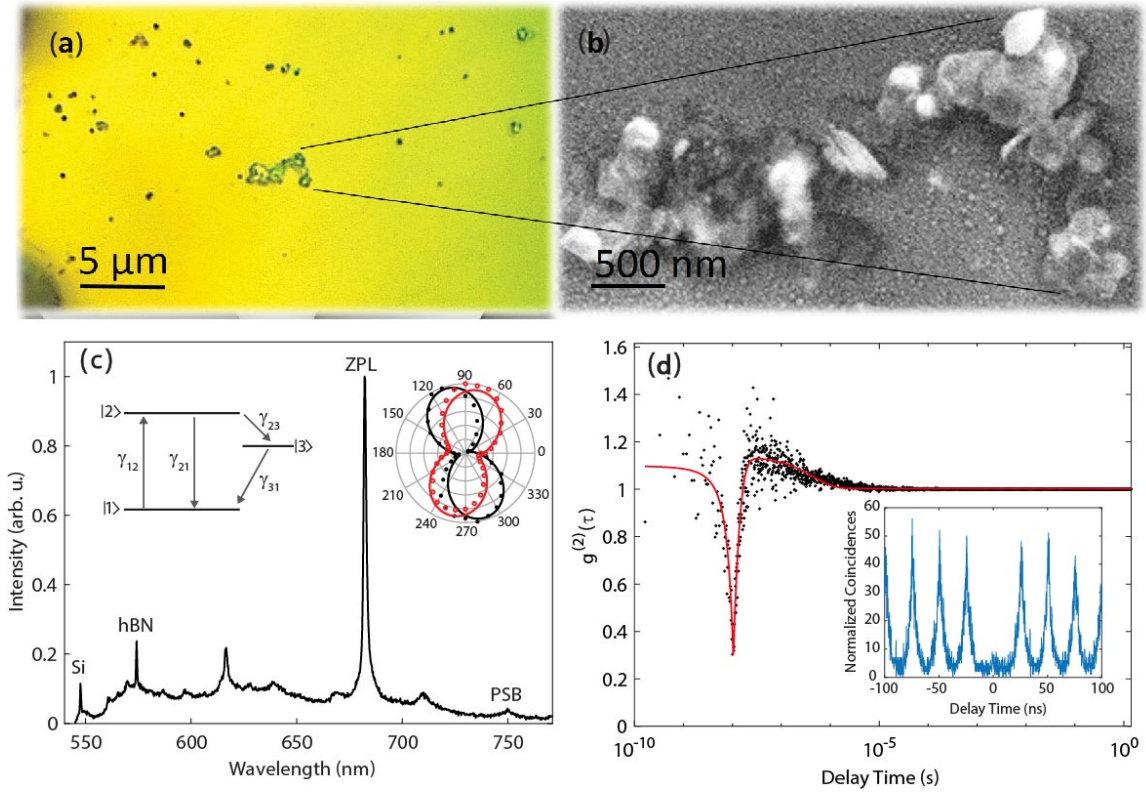


FIG. 1. (a) Optical microscope image of the sample surface showing hBN flakes on a silicon substrate. (b) SEM image of selected bulk hBN flakes from the region shown in (a). (c) A representative photoluminescence (PL) spectrum acquired from an hBN flake, showing Raman scattering peaks from both the silicon substrate and the hBN structure, along with a bright zero-phonon line (ZPL) emission from a single defect at 684 nm. (Inset) Polarization dependence of the ZPL emission: excitation (filled circles) and emission (open circles). (d) Second-order photon correlation measurements of the ZPL emission under both continuous-wave (CW) and pulsed excitation at room temperature.

sured the second-order photon correlation function  $g^{(2)}(\tau)$  using a Hanbury-Brown and Twiss (HBT) setup comprising a 50:50 beamsplitter and two single-photon counting modules (SPCMs), with timing recorded via a multichannel time-stamping unit. Figure 1d shows the histogram of detection time delays under CW excitation. The pronounced antibunching dip at zero delay with  $g^{(2)}(0) = 0.3$  confirms the single-photon nature of the emission. The observed bunching behavior indicates a three-level system, a feature commonly observed in solid-state quantum emitters, including defects in hBN [39] and diamond [42]. A schematic of the emitter's level structure is shown in the inset of Fig. 1c. It includes a ground state  $|1\rangle$ , an excited state  $|2\rangle$ , and a metastable shelving state  $|3\rangle$ . The relevant transition rates are denoted as follows:  $\gamma_{12}$  (excitation),  $\gamma_{21}$  (radiative  $\gamma_r$  and nonradiative  $\gamma_{nr}$  decay),  $\gamma_{23}$  (shelving), and  $\gamma_{31}$  (deshelving). These rates govern the dynamics and intensity of the ZPL emission. The deviation of  $g^{(2)}(0)$  from the ideal value of zero is attributed to imperfect spectral filtering of the ZPL and the limited temporal resolution of the HBT system (approximately 400 ps), which is insufficient to fully resolve fast decay processes governed by  $\gamma_{21}$  and  $\gamma_{12}$ . To mitigate these limitations, we also performed photon correlation measurements under pulsed excitation at 483 nm. Under these conditions, a much stronger suppression of the peak at the zero time-delay is observed, with an

antibunching value of  $g^{(2)}(0) = 0.1$ , as shown in the inset of Fig. 1d).

In order to investigate the effect of Ag nanoantennas on the optical properties of single defects in hBN, the nanoantennas were fabricated in the vicinity of the defects using a self-organized approach, rather than moving the defect centers close to pre-fabricated antennas [19]. For this, a technique called solid-state dewetting of thin films was employed. A 5/13 nm thick Ag film was deposited on the hBN-coated silicon substrate and subsequently annealed at approximately 350 °C [43–45]. Silver was chosen due to its low optical loss, strong and narrow plasmonic resonance bands, and superior dewetting properties compared to other noble metals such as gold. By controlling the dewetting duration, the size distribution of the resulting nanoantennas can be tuned (Supporting Information Figure S1).

During the annealing process, the thin Ag film becomes unstable at temperatures well below the melting point of silver due to a high surface-area-to-volume ratio [46]. To minimize this instability, silver atoms diffuse and agglomerate, leading to the formation of nano-sized islands as presented in Figure 2a. These nanoislands take on a largely hemispheroidal shape, resulting in Ag nanoantennas distributed across the hBN flakes as well as on the silicon substrate. Because the dewetting process is stochastic, nanoantennas also form in

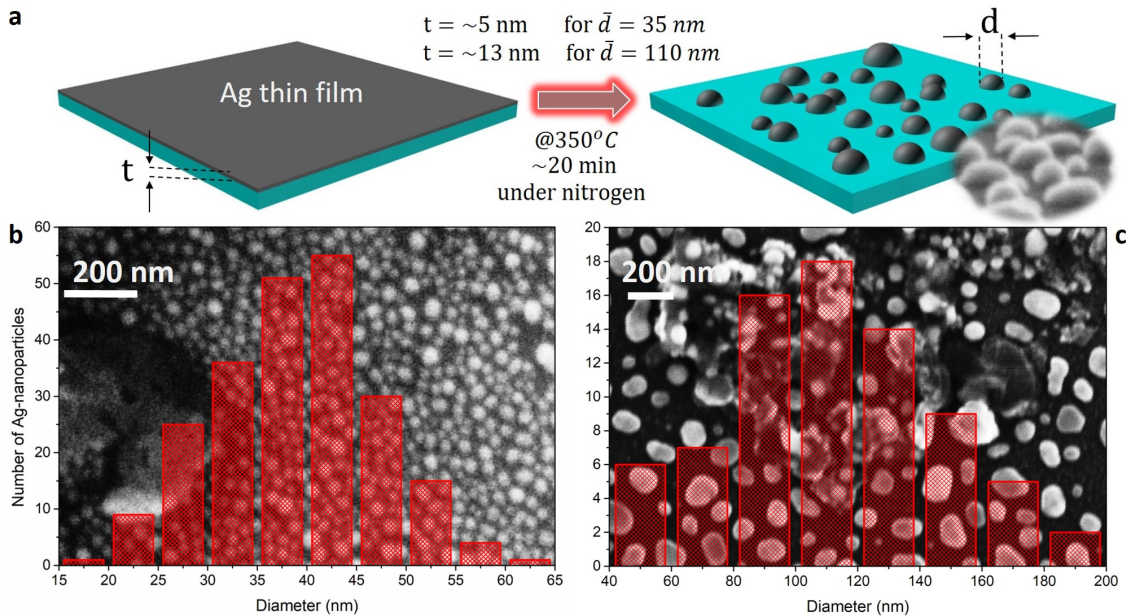


FIG. 2. (a) Schematic illustrating the fabrication of hemispherical Ag nanoparticles via dewetting of a Ag thin film on a  $\text{SiO}_2/\text{Si}$  substrate. (b) Size distribution histogram and corresponding electron microscope image of smaller AgNPs with an average diameter around 40 nm, used for fluorescence quenching. (c) Size distribution histogram and corresponding electron microscope image of larger AgNPs with an average diameter around 110 nm, used for fluorescence enhancement.

close proximity to defect centers.

The fabrication process consists of two steps: vacuum thermal metal evaporation followed by thermal annealing in a nitrogen environment. This method is gentle on both the hBN flakes and the silicon substrate, which are stable up to  $\sim 800^\circ\text{C}$  [47]. By controlling the initial Ag film thickness, the size distribution of the resulting nanoantennas can be tuned. In this work, 5 nm and 13 nm thick films produced nanoantennas with average diameters of approximately 35 nm and 110 nm, respectively (Figure 2b and c). These size regimes were selected to demonstrate both quenching and enhancement effects on the fluorescence of single defects in hBN, as the size of Ag nanoantennas strongly influences their absorption and scattering properties [48].

#### A. AgNPs on hBN: Emitter Characterization and Plasmonic Coupling

Figure 3a shows PL spectra from a local spot of an hBN sample taken under similar excitation conditions (power and polarization) before and after the fabrication of small AgNPs (35 nm in diameter). The bright peaks at 562 nm and 663 nm are identified as ZPL emission from two defects, and the broad doublets around 610 nm and 740 nm correspond to their associated PSBs, arising from coupling to optical phonons of the host hBN—specifically, the Raman-active phonon at  $1370\text{ cm}^{-1}$  and the IR-active phonon at  $1600\text{ cm}^{-1}$ . A small peak at 574 nm appears only in the spectrum with AgNPs and is attributed to the Raman scattering of hBN. The influence of AgNPs is clearly observed as strong quenching in

the emission from both defects, affecting both ZPLs and their PSBs. This quenching is particularly pronounced for the ZPL at 562 nm, likely due to better spectral overlap with the localized surface plasmon resonance of the AgNPs. The observed reduction in emission intensity is attributed to enhanced non-radiative decay channels introduced by the proximity of the AgNPs, which facilitate energy transfer from the emitter to the metal nanoparticle. For further analysis, we focus on the defect emitting at 663 nm, as its emission line is more spectrally isolated and thus more suitable for quantitative characterization.

To investigate the origin of the observed quenching in PL emission under identical excitation conditions, power-dependent PL measurements were conducted on the same defect emitting at 663 nm, both before and after AgNP fabrication. From each spectrum, the intensity of the ZPL emission and the hBN Raman scattering were extracted and are shown in Figure 3b for quantitative comparison. While the Raman signal is visible only at high excitation powers, it exhibits a linear power dependence, consistent with its scattering origin. Notably, a clear enhancement in the Raman scattering is observed after the AgNP formation, attributed to surface-enhanced Raman scattering (SERS) [49–51]. In contrast, the ZPL intensity shows typical saturation behavior. At low excitation powers, the ZPL intensity  $I$  increases linearly with power, following  $I \approx \gamma_{12} \times QE$ , where  $\gamma_{12}$  is the excitation rate and  $QE$  is the quantum efficiency. At higher excitation powers, saturation sets in, and the intensity reaches a maximum limited by the radiative and non-radiative decay rates, as well as the involvement of metastable triplet states. In this regime, the PL intensity can be de-

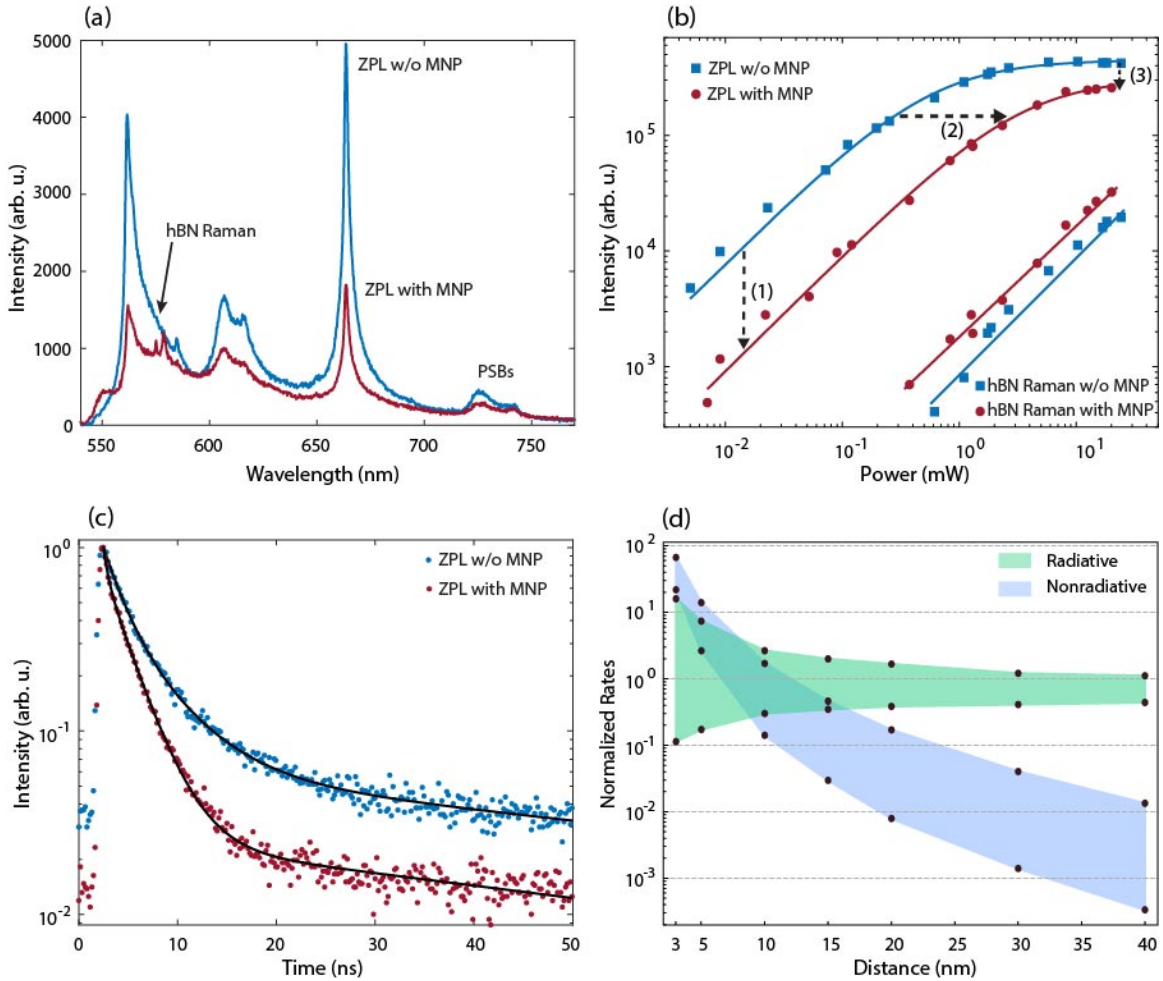


FIG. 3. (a) PL spectra of a single defect in hBN with a ZPL at 663 nm, measured before and after the deposition of Ag nanoantennas. PSBs appear around 730 nm, while the peak at 574 nm corresponds to Raman scattering of hBN. A significant quenching of ZPL intensity is observed after Ag deposition. (b) Excitation power-dependent intensities of the ZPL and hBN Raman scattering before and after Ag nanoantenna formation. ZPL emission shows strong quenching, while the Raman peak is enhanced due to near-field enhancement effects. (c) Time-resolved PL measurements showing a clear reduction in lifetime after Ag nanoantenna formation, indicating enhanced total decay rate due to coupling with plasmonic modes. (d) FDTD simulation results for a model system consisting of a defect in hBN coupled to a 40 nm diameter Ag nanoparticle. Radiative and non-radiative decay rates are plotted as functions of emitter–nanoparticle distance. Radiative enhancement dominates at intermediate distances, while non-radiative decay sharply increases at shorter separations. Higher modification is observed for dipoles oriented parallel to the Ag surface, while lower rates occur for orthogonal dipole orientations as shown in the shaded regions.

scribed by  $I = \gamma_r \gamma_{31} / (\gamma_{31} + \gamma_{23})$ , where  $\gamma_r$  is the radiative decay rate, and  $\gamma_{23}, \gamma_{31}$  are the intersystem crossing rates associated with the triplet states. The quantum efficiency, defined as  $QE = \gamma_r / (\gamma_{nr} + \gamma_r + \gamma_{23})$  reflects the competition between radiative decay ( $\gamma_r$ ), non-radiative decay ( $\gamma_{nr}$ ), and intersystem crossing. The significant quenching observed after AgNP fabrication is consistent with an increase in non-radiative decay pathways, likely caused by energy transfer from the emitter to the nearby metallic nanoparticle, which reduces the  $QE$ .

The saturation profile of the ZPL emission reveals three significant changes upon coupling to the small AgNPs. First, under weak excitation conditions, the ZPL intensity exhibits a quenching factor of approximately 8.4, indicating a strong reduction in the quantum efficiency of the emitter. This

low-power behavior arises from a combination of field enhancement and modifications to the emitter’s decay dynamics. Specifically, the enhancement of the non-radiative decay rate outweighs enhancements in both the excitation and radiative decay rates, a well-established effect for small AgNPs near quantum emitters [48]. Second, the excitation power required to reach the saturation regime increases by nearly a factor of 6 after AgNP coupling. This is consistent with an increase in the total decay rate, as saturation intensity is reached when the excitation rate  $\gamma_{12}$  becomes comparable to the sum of the decay channels. The AgNP-induced modification accelerates the decay processes, necessitating higher excitation power to achieve saturation. Finally, at excitation powers well above saturation, the ZPL intensity still shows a  $\sim 40\%$  reduction

compared to the uncoupled case. Since the saturation intensity is primarily determined by the radiative decay rate, this observation implies that coupling to the AgNP leads to a reduced radiative decay rate. Together, these results demonstrate that the presence of a small AgNP strongly modifies both radiative and non-radiative processes, ultimately diminishing the quantum efficiency and emission intensity of the defect.

Time-resolved photoluminescence measurements (Figure 3c) and FDTD simulations (Figure 3d) further corroborate the impact of AgNPs on the emitter's decay dynamics. The decay rate modifications are quantified using time-correlated single-photon counting (TCSPC), with representative decay curves shown in Figure 3c. After AgNP formation, the fluorescence decay accelerates noticeably, consistent with an increase in total decay rates due to plasmonic coupling. The decay curves are fitted with a bi-exponential function, yielding two characteristic time constants,  $\tau_1$  and  $\tau_2$ . While these components are often associated with distinct physical processes—such as radiative decay from the excited singlet state and population dynamics involving a metastable triplet state—their exact interpretation requires caution. In a three-level emitter system, both  $\tau_1$  and  $\tau_2$  are effective time constants that reflect contributions from multiple decay channels, including radiative, non-radiative, and intersystem crossing processes. In this context, the faster component  $\tau_1$  decreases significantly from 1.87 ns to 0.80 ns, indicating a substantial increase in the total decay rate of the excited state. The slower component  $\tau_2$  also shortens from 5.3 ns to 2.89 ns, suggesting that the dynamics of long-lived states, such as the triplet manifold, are also altered, possibly due to changes in intersystem crossing efficiency or enhanced relaxation through modified photonic or non-radiative channels induced by the nearby AgNPs.

Complementary FDTD simulations further support these findings by calculating radiative and non-radiative decay rates as a function of emitter–nanoparticle separation and particle size. As shown in Figure 3d, these simulations illustrate how a nearby AgNP (with a diameter of 40 nm) alters the emitter's decay dynamics. The shaded regions in the plots represent the range of rate modifications arising from the orientation of the emitter's dipole moment relative to the nanoparticle surface, ranging from a dipole aligned *parallel* to the nanoparticle surface (strongest coupling) to one oriented *orthogonally* (weakest coupling). This variation establishes upper and lower bounds for both radiative and non-radiative decay rate enhancements. At emitter–nanoparticle separations less than 10 nm, strong non-radiative enhancement dominates due to energy transfer into lossy plasmon modes of the metal, leading to fluorescence quenching. These effects are more pronounced for dipoles oriented orthogonally to the nanoparticle surface, which couple less efficiently to radiative modes and more strongly to non-radiative channels. Overall, the simulation results are in good agreement with experimental observations of lifetime shortening and emission quenching.

To complement the quenching behavior induced by small AgNPs, we investigate the impact of coupling hBN quantum emitters to larger AgNPs with diameters exceeding 100 nm. Unlike smaller AgNPs, which primarily increase non-

radiative losses due to their high absorption cross-sections, larger particles exhibit stronger scattering and support more favorable conditions for radiative enhancement. These nanoparticles can sustain localized surface plasmon resonances that efficiently couple with nearby emitters, modifying the local density of optical states (LDOS) and enhancing the radiative decay channel. As shown in Figure 4a, PL spectra obtained before and after AgNP formation reveal a substantial increase in emission intensity from a single defect. The ZPL of the emitter, located at 616 nm, becomes nearly five times more intense following AgNP deposition, and the PSB around 670 nm is significantly more pronounced. These enhancements are indicative of improved radiative recombination pathways facilitated by plasmonic coupling. Importantly, this increase in emission is not accompanied by spectral distortion or shifts in the emission peaks, suggesting that the local electromagnetic environment is modified without compromising the spectral identity of the defect.

Power-dependent PL measurements, displayed in Figure 4b, further support this interpretation. Although the saturation power remains nearly unchanged compared to the pre-coupling condition, the maximum achievable PL intensity increases markedly, indicating an improvement in the radiative quantum efficiency of the emitter. This behavior is in stark contrast to the quenching observed with smaller AgNPs, where both the emission intensity and saturation behavior were adversely affected. In this case, the nearly unchanged excitation threshold alongside enhanced PL intensity implies a selective amplification of the radiative decay rate without a significant increase in non-radiative losses.

Time-resolved measurements shown in Figure 4c reveal that the ZPL emission at 616 nm initially exhibits a single-exponential decay with a lifetime of  $\tau_1 = 20$  ns. After coupling to the large AgNP, the decay becomes bi-exponential, with  $\tau_1 = 0.12$  ns and  $\tau_2 = 8.4$  ns, indicating a substantial increase in the total decay rate due to strong plasmonic coupling. Despite this dramatic lifetime shortening, the observed PL enhancement is approximately fivefold (Figure 4a–b), which appears modest by comparison. This discrepancy arises because lifetime measurements reflect the total decay rate, including both radiative and non-radiative channels, while PL intensity depends primarily on the radiative rate and the emitter's quantum efficiency. Non-radiative losses, changes in emission directivity, and collection efficiency can all limit the net PL enhancement, even when lifetime shortening is substantial. These results demonstrate that large AgNPs can effectively enhance the radiative properties of quantum emitters in hBN, offering a promising route for plasmon-assisted brightness enhancement without significant spectral distortion.

The FDTD simulations, shown in Figure 4d, indicate that at emitter–NP separations of approximately 10–25 nm, the radiative decay rate is significantly enhanced, while non-radiative rates remain comparatively low. This favorable regime supports efficient photon emission and aligns well with the experimental PL and lifetime results. Additionally, the enhancement exhibits strong dependence on dipole orientation: emitters with dipole moments parallel to the nanoparticle surface couple more efficiently to the plasmonic mode, resulting

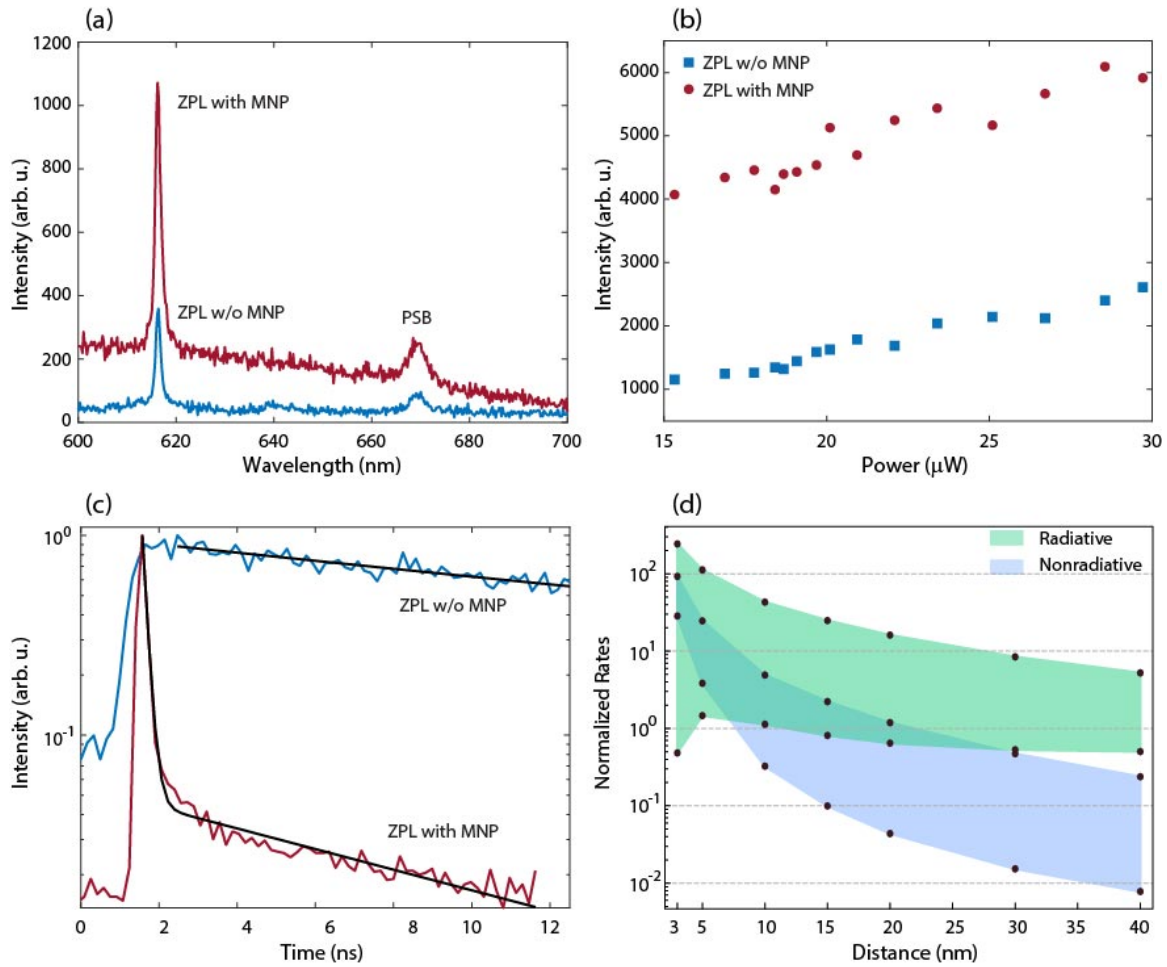


FIG. 4. (a) PL Spectra of a defect with ZPL at 616 nm before and after the metal nanoparticle taken at similar excitation conditions. Broad peaks around 670 nm are the corresponding PSBs of the defect emission. (b) Excitation power-dependent ZPL intensity before and after the fabrication of AgNPs. A strong fluorescence enhancement is observed. (c) The result of time-resolved measurements on the ZPL emission before and after the AgNPs shows a strong decay time enhancement. (d) Results of FDTD simulations on an ideal system where a defect in hBN is coupled to a small AgNP with a diameter of 120 nm. Modifications on both radiative and non-radiative rates as a function of emitter-AgNP distance are clearly visible.

in greater Purcell enhancement compared to orthogonal orientations.

These results establish a clear nanoparticle size-dependent behavior in the plasmonic coupling of hBN quantum emitters. Engineering the size and geometry of metal nanoparticles thus offers a powerful means to tailor light-matter interactions in two-dimensional quantum photonic systems. Moreover, the observed changes in decay dynamics suggest that plasmonic coupling not only modifies radiative and non-radiative decay pathways, but also perturbs metastable triplet states. This can alter excited-state population dynamics and saturation behavior, consistent with plasmon-mediated control of excited-state kinetics reported in other solid-state emitters [52].

## B. Hybrid Nanocavities on Gold/Silicon Dioxide: Enhanced Uniformity and Confinement

In the second phase of this study, building upon the emission enhancement observed via thermally dewetted AgNPs, we developed a hybrid cavity platform to further improve the enhancement of emission from defects in hBN nanoflakes. This platform consists of a metal-dielectric Au/SiO<sub>2</sub> bilayer substrate combined with self-assembled AgNPs. Two parameters of the hybrid cavity platform, SiO<sub>2</sub> and Au layer thicknesses, are investigated by FDTD simulations, and the thickness values of 20 nm and 100 nm are determined for SiO<sub>2</sub> and Au mirror layer for the fabrication process, respectively. Scattering cross-section simulation results for the hybrid cavity with different thickness values can be found in the Supporting Information, Figures S2 and S3.

The plasmonic nanostructures were formed by the same thermal dewetting method using silver films of varying thick-

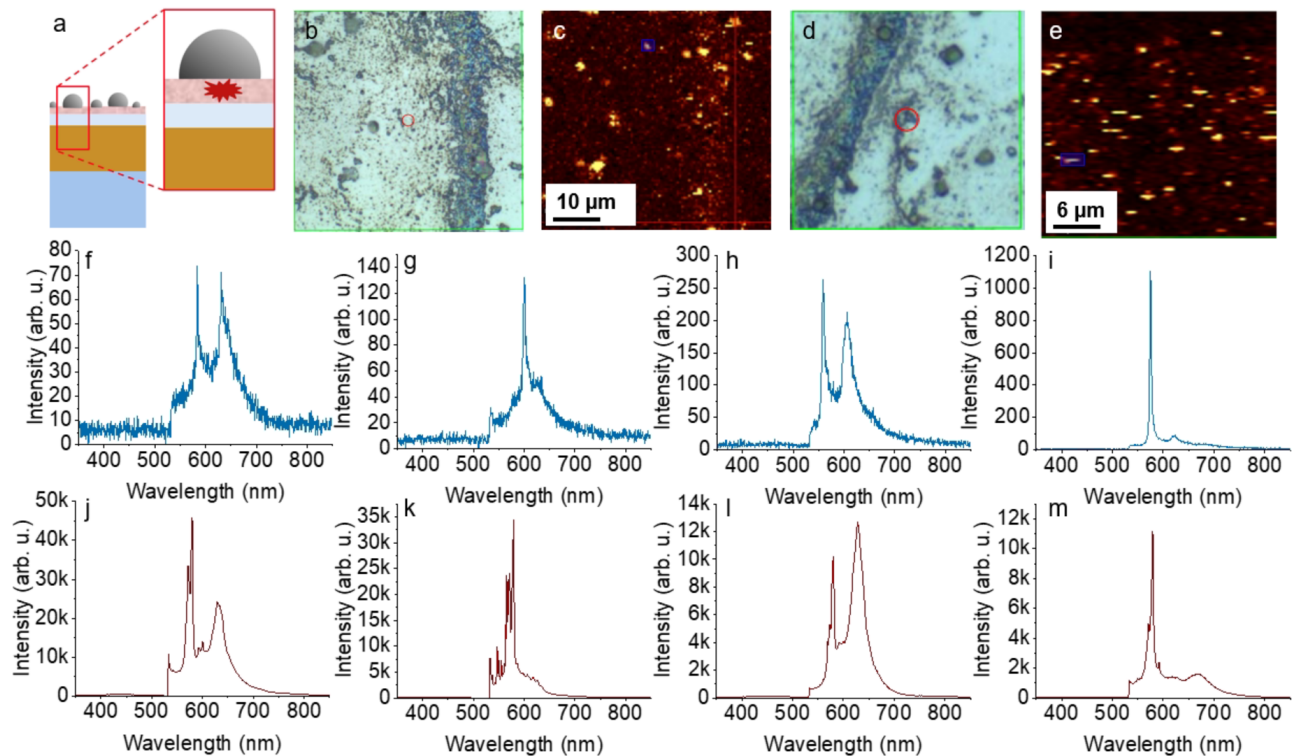


FIG. 5. (a) Simulated structure (not to scale), images of hBN without plasmonic nanocavity on the (b) conventional bright-field microscope and (c) confocal laser scanning microscope (CLSM), images of hBN with plasmonic nanocavity on the (d) conventional bright-field microscope, and (e) CLSM. The spectrum of hBN defect emissions at different wavelengths (f-i) without and (j-m) with plasmonic nanocavity.

nesses (5–13 nm). The dewetting temperature is significantly lower than the stability threshold of the Au/SiO<sub>2</sub> bilayer, the Si substrate, and the hBN flakes, ensuring structural integrity throughout processing. When AgNPs are formed on hBN flakes supported by Au/SiO<sub>2</sub> substrates, the resulting vertical nanocavity—comprising the AgNP, hBN layer, and reflective Au film—provides enhanced field confinement and optical feedback. This configuration enables strong plasmonic interactions without complex alignment or lithography, addressing key limitations of conventional cavity designs in terms of scalability and reproducibility.

Figure 5 presents (a) simulated structure (not to scale), (b) and (d) conventional bright-field microscope images in panels, and (c) and (e) fluorescence imaging in panels for samples without and with AgNPs, respectively. Panels 5 (f-i) show the PL counts from hBN flakes prior to AgNP formation. After the thermal dewetting process and formation of AgNPs, the PL intensities increased by approximately 100-fold, as shown in panels (j-m). Four distinct measurements exhibiting emissions with consistent spectral features were compared in this study. These emissions arise from randomly selected emitters, since tracking the exact same emitter before and after dewetting was not feasible.

Through plasmonic coupling, the AgNPs significantly enhance emission intensity and modulate the spectral response of hBN emitters. The interaction between the defects, the spacer layers, and localized surface plasmons introduces both field enhancement and spectral reshaping, producing a range

of emission profiles depending on the defect type and local environment. These effects manifest as distinct ZPL and PSB features at different wavelengths, reflecting the heterogeneous nature of hBN’s defect states. Importantly, the observed PL enhancement spans the full spectral range of the emitters, underscoring the broadband capability of the proposed platform.

### III. CONCLUSION

This study establishes a powerful and scalable platform for engineering light–matter interactions at the nanoscale by integrating stochastic plasmonic nanocavities with quantum emitters in hBN. Through thermal dewetting of noble metal films, we demonstrate a deterministic-free fabrication route that yields strong and tunable coupling by-design between defect centers and plasmonic nanoantennas achieving photoluminescence enhancements of up to two orders of magnitude. This result firmly establishes these hybrid structures as efficient single photon sources for applications in quantum technologies, i.e. quantum key distribution [53–56]. Our results reveal how local field confinement, decay rate manipulation, and cavity-emitter synergy can be harnessed without complex nanofabrication or precise emitter positioning.

Beyond the demonstrated optical control, this platform paves the way for transformative advances in quantum photonic technologies. Its simplicity, material compatibility, and

spectral versatility make it a promising candidate for integration on next-generation on-chip quantum circuits and room-temperature nanoscale quantum sensors as tunable and bright single-photon sources. In particular, the ability to construct high-efficiency quantum nanoantennas on 2D materials such as hBN opens up unexplored opportunities for label-free single-molecule detection, quantum-enhanced sensing, and hybrid photonic-bio interfaces [57].

#### IV. EXPERIMENTAL SECTION

Multilayer hBN flakes were obtained commercially in solution form (Graphene Supermarket) and drop-casted ( $\approx 10 \mu\text{L}$ ) on a silicon substrate, which has laser engraved marks to locate specific emitters before and after the fabrication of AgNPs.

hBN defect centers are excited by a CW laser ( $\lambda_{exc}=532 \text{ nm}$ , Verdi-V6 Coherent) and a pulsed diode laser ( $\lambda_{exc}=483 \text{ nm}$ , 65 ps pulse width, Advanced Laser Diode Systems). Fluorescence is collected using a 50X/0.75 NA objective (Optika). The optimum polarization angle of the excitation is deter-

mined using a motorized half-waveplate (HWP). In the detection part of the setup, the Rayleigh scattered light is rejected with a 540 nm notch filter. The sample surface is imaged by a CMOS camera white light illumination. A spectrometer (Andor Shamrock 750) is employed with an EMCCD camera (Andor Newton). The lifetime measurement of the quantum emitter is performed by a photon counting avalanche photodiode (APD) mounted on the HBT interferometer. APDs are connected to a time tagging electronic module (TTM8000, Roithner Laser Technik).

#### Supporting Information

Supporting Information is available from the Wiley Online Library or from the author.

#### Acknowledgments

The authors thank Selcuk Yerci for the workstation on which we performed our computations and Vasilis Karanikolas for reviewing some of the calculations. S. G. acknowledges the Middle East Technical University Postdoctoral Research Program (DOSAP-B). S. A. acknowledges the support of the Türkiye Scientific and Technological Research Council (TÜBİTAK) under project number 118F119.

- 
- [1] A. M. Fox, *Advanced Quantum Technologies* **8**, 2300390 (2025).
- [2] M. Kianinia, Z.-Q. Xu, M. Toth, and I. Aharonovich, *Applied Physics Reviews* **9**, 011306 (2022), [https://pubs.aip.org/aip/apr/article-pdf/doi/10.1063/5.0072091/19805142/011306\\_1\\_online.pdf](https://pubs.aip.org/aip/apr/article-pdf/doi/10.1063/5.0072091/19805142/011306_1_online.pdf).
- [3] G. Grosso, H. Moon, B. Lienhard, S. Ali, D. K. Efetov, M. M. Furchi, P. Jarillo-Herrero, M. J. Ford, I. Aharonovich, and D. Englund, *Nature Communications* **8**, 705 (2017).
- [4] H. Herzig Sheinfux, L. Orsini, M. Jung, I. Torre, M. Ceccanti, S. Marconi, R. Maniyara, D. Barcons Ruiz, A. Hötger, R. Bertini, S. Castilla, N. C. H. Hesp, E. Janzen, A. Holleitner, V. Pruneri, J. H. Edgar, G. Shvets, and F. H. L. Koppens, *Nature Materials* **23**, 499 (2024).
- [5] K. Yamamura, N. Coste, H. Z. J. Zeng, M. Toth, M. Kianinia, and I. Aharonovich, *Nanophotonics* doi:10.1515/nanoph-2024-0412 (2024).
- [6] M. K. Prasad, M. P. C. Taverne, C.-C. Huang, J. D. Mar, and Y.-L. D. Ho, *Materials* **17**, 10.3390/ma17164122 (2024).
- [7] T. T. Tran, K. Bray, M. J. Ford, M. Toth, and I. Aharonovich, *Nature Nanotechnology* **11**, 37 (2016).
- [8] A. Çakan, C. Cholsuk, A. Gale, M. Kianinia, S. Paçal, S. Ateş, I. Aharonovich, M. Toth, and T. Vogl, *Advanced Optical Materials* **13**, 2402508 (2025).
- [9] M. Hennessey, B. Whitefield, A. Gale, M. Kianinia, J. A. Scott, I. Aharonovich, and M. Toth, *Advanced Quantum Technologies* , 2300459 (2024), <https://onlinelibrary.wiley.com/doi/pdf/10.1002/qute.202300459>.
- [10] M. Nonahal, C. Li, H. Ren, L. Spencer, M. Kianinia, M. Toth, and I. Aharonovich, *Laser & Photonics Reviews* **17**, 2300019 (2023).
- [11] C. Li, J. E. Fröch, M. Nonahal, T. N. Tran, M. Toth, S. Kim, and I. Aharonovich, *ACS Photonics* **8**, 2966 (2021).
- [12] S. Kim, J. E. Fröch, J. Christian, M. Straw, J. Bishop, D. Totonjian, K. Watanabe, T. Taniguchi, M. Toth, and I. Aharonovich, *Nature Communications* **9**, 2623 (2018).
- [13] P. K. Shandilya, J. E. Fröch, M. Mitchell, D. P. Lake, S. Kim, M. Toth, B. Behera, C. Healey, I. Aharonovich, and P. E. Barclay, *Nano Letters* **19**, 1343 (2019), <https://doi.org/10.1021/acs.nanolett.8b04956>.
- [14] T. T. Tran, D. Wang, Z.-Q. Xu, A. Yang, M. Toth, T. W. Odom, and I. Aharonovich, *Nano Letters* **17**, 2634 (2017), <https://doi.org/10.1021/acs.nanolett.7b00444>.
- [15] N. Mendelson, Z.-Q. Xu, T. T. Tran, M. Kianinia, J. Scott, C. Bradac, I. Aharonovich, and M. Toth, *ACS Nano* **13**, 3132 (2019), <https://doi.org/10.1021/acs.nano.8b08511>.
- [16] E. M. Purcell, Spontaneous emission probabilities at radio frequencies, in *Confined Electrons and Photons: New Physics and Applications*, edited by E. Burstein and C. Weisbuch (Springer US, Boston, MA, 1995) pp. 839–839.
- [17] H. Megahd, D. Comoretto, and P. Lova, *Optical Materials: X* **13**, 100130 (2022).
- [18] X.-D. Zeng, Y.-Z. Yang, N.-J. Guo, Z.-P. Li, Z.-A. Wang, L.-K. Xie, S. Yu, Y. Meng, Q. Li, J.-S. Xu, W. Liu, Y.-T. Wang, J.-S. Tang, C.-F. Li, and G.-C. Guo, *Nanoscale* **15**, 15000 (2023).
- [19] M. Nguyen, S. Kim, T. T. Tran, Z.-Q. Xu, M. Kianinia, M. Toth, and I. Aharonovich, *Nanoscale* **10**, 2267 (2018).
- [20] D. Gérard, A. Pierret, H. Fartas, B. Berini, S. Buil, J.-P. Hermier, and A. Delteil, *ACS Photonics* **11**, 5188 (2024), 2407.20160.
- [21] X. Xu, A. B. Solanki, D. Sychev, X. Gao, S. Peana, A. S. Baburin, K. Pagadala, Z. O. Martin, S. N. Chowdhury, Y. P. Chen, T. Taniguchi, K. Watanabe, I. A. Rodionov, A. V. Kildishev, T. Li, P. Upadhyaya, A. Boltasseva, and V. M. Shalaev, *Nano Letters* **23**, 25–33 (2022).
- [22] V. Karanikolas, T. Iwasaki, J. Henzie, N. Ikeda, Y. Yamauchi, Y. Wakayama, T. Kuroda, K. Watanabe, and T. Taniguchi, *ACS Omega* **8**, 14641 (2023), <https://doi.org/10.1021/acsomega.3c00512>.
- [23] M. Dowran, A. Butler, S. Lamichhane, A. Erickson, U. Kilic,

- S.-H. Liou, C. Argyropoulos, and A. Laraoui, *Advanced Optical Materials* **11**, 2300392 (2023).
- [24] A. I. Barreda, M. Zapata-Herrera, I. M. Palstra, L. Mercadé, J. Aizpurua, A. F. Koenderink, and A. Martínez, *Photon. Res.* **9**, 2398 (2021).
- [25] M. Zhang, C. I. Lozano, S. van Veen, and L. Albertazzi, arXiv, 2409.18702 (2024), arXiv:2409.18702 [cond-mat.mes-hall].
- [26] S. Hu, M. Khater, R. Salas-Montiel, E. Kratschmer, S. Engelmann, W. M. J. Green, and S. M. Weiss, *Science Advances* **4**, eaat2355 (2018), <https://www.science.org/doi/pdf/10.1126/sciadv.aat2355>.
- [27] U. Khalil, W. Farooq, J. Iqbal, S. Z. Kazmi, A. Khan, A. Rehman, and S. Ayub, *European Physical Journal Plus* **136** (2021).
- [28] P. A. Dmitriev, E. Lassalle, L. Ding, Z. Pan, D. C. J. Neo, V. Valuckas, R. Paniagua-Dominguez, J. K. W. Yang, H. V. Demir, and A. I. Kuznetsov, *ACS Photonics* **10**, 582 (2023), <https://doi.org/10.1021/acsp Photonics.2c01332>.
- [29] Y. Meng, H. Zhong, Z. Xu, T. He, J. S. Kim, S. Han, S. Kim, S. Park, Y. Shen, M. Gong, Q. Xiao, and S.-H. Bae, *Nanoscale Horizons* **8**, 1345 (2023).
- [30] S. Yan, X. Zhu, J. Dong, Y. Ding, and S. Xiao, *Nanophotonics* **9**, 1877 (2020).
- [31] S. K. Patel and C. Argyropoulos, *EPJ Applied Metamaterials* **2**, 4 (2015).
- [32] I. S. Maksymov, I. Staude, A. E. Miroshnichenko, and Y. S. Kivshar, *Nanophotonics* **1**, 65 (2012).
- [33] T. Coenen, F. Bernal Arango, A. Femius Koenderink, and A. Polman, *Nature Communications* **5**, 3250 (2014).
- [34] J. E. Fröch, L. P. Spencer, M. Kianinia, D. D. Totonjian, M. Nguyen, A. Gottscholl, V. Dyakonov, M. Toth, S. Kim, and I. Aharonovich, *Nano Letters* **21**, 6549 (2021), pMID: 34288695, <https://doi.org/10.1021/acs.nanolett.1c01843>.
- [35] S. Häußler, G. Bayer, R. Waltrich, N. Mendelson, C. Li, D. Hunger, I. Aharonovich, and A. Kubanek, *Advanced Optical Materials* **9**, 2002218 (2021), <https://onlinelibrary.wiley.com/doi/pdf/10.1002/adom.202002218>.
- [36] T. Kuzuba, K. Era, T. Ishii, and T. Sato, *Solid State Communications* **25**, 863 (1978).
- [37] R. J. Nemanich, S. A. Solin, and R. M. Martin, *Phys. Rev. B* **23**, 6348 (1981).
- [38] O. Arı, N. Polat, V. Firat, Ö. Çakır, and S. Ateş, *ACS Photonics* **12**, 1676 (2025).
- [39] T. T. Tran, K. Bray, M. J. Ford, M. Toth, and I. Aharonovich, *Nature Nanotechnology* **11**, 37 (2015).
- [40] N. R. Jungwirth and G. D. Fuchs, *Phys. Rev. Lett.* **119**, 057401 (2017).
- [41] A. Kumar, Ç. Samaner, C. Cholsuk, T. Matthes, S. Paçal, Y. Oyun, A. Zand, R. J. Chapman, G. Saerens, R. Grange, S. Suwanna, S. Ateş, and T. Vogl, *ACS Nano* **18**, 5270 (2024).
- [42] C. Kurtsiefer, S. Mayer, P. Zarda, and H. Weinfurter, *Phys. Rev. Lett.* **85**, 290 (2000).
- [43] E. Jiran and C. V. Thompson, *Journal of Electronic Materials* **19**, 1153 (1990).
- [44] M. Z. Borra, S. K. Güllü, F. Es, O. Demircioğlu, M. Günöven, R. Turan, and A. Bek, *Applied Surface Science* **318**, 43 (2014).
- [45] H. Nasser, Z. M. Saleh, E. Özkol, M. Günöven, A. Bek, and R. Turan, *Plasmonics* **8**, 1485 (2013).
- [46] E. Jiran and C. Thompson, *Thin Solid Films* **208**, 23 (1992).
- [47] M. Kianinia, B. Regan, S. A. Tawfik, T. T. Tran, M. J. Ford, I. Aharonovich, and M. Toth, *ACS Photonics* **4**, 768 (2017).
- [48] J. R. Lakowicz, *Analytical Biochemistry* **337**, 171 (2005).
- [49] M. Fleischmann, P. Hendra, and A. McQuillan, *Chemical Physics Letters* **26**, 163 (1974).
- [50] D. L. Jeanmaire and R. P. Van Duyne, *Journal of Electroanalytical Chemistry and Interfacial Electrochemistry* **84**, 1 (1977).
- [51] K. Kneipp, Y. Wang, H. Kneipp, L. T. Perelman, I. Itzkan, R. R. Dasari, and M. S. Feld, *Phys. Rev. Lett.* **78**, 1667 (1997).
- [52] Y. Wang, M. Horáček, and P. Zijlstra, *The Journal of Physical Chemistry Letters* **11**, 1962 (2020).
- [53] F. Wang, N. Cooper, D. Johnson, B. Hopton, T. M. Fromhold, R. Hague, A. Murray, R. McMullen, L. Turyanska, and L. Hackermüller, *Additive manufacturing for advanced quantum technologies* (2025), arXiv:2503.11570 [physics.app-ph].
- [54] Ç. Samaner, S. Paçal, G. Mutlu, K. Uyanık, and S. Ateş, *Advanced Quantum Technologies* **5**, 2200059 (2022).
- [55] A. Al-Juboori, H. Z. J. Zeng, M. A. P. Nguyen, X. Ai, A. Laucht, A. Solntsev, M. Toth, R. Malaney, and I. Aharonovich, *Advanced Quantum Technologies* **6**, 2300038 (2023).
- [56] Ö. S. Tapşın, F. Ağlarıcı, R. G. Pousa, D. K. L. Oi, M. Gündoğan, and S. Ateş, arXiv 10.48550/arxiv.2501.13902 (2025), 2501.13902.
- [57] C. Couteau, S. Barz, T. Durt, T. Gerrits, J. Huwer, R. Prevedel, J. Rarity, A. Shields, and G. Weihs, *Nature Reviews Physics* **5**, 354 (2023).